PAPER

Check for updates

Coarse-grained force-field for large scale molecular dynamics simulations of polyacrylamide and polyacrylamide-gels based on quantum mechanics†

Mei Zheng,[ab] Andres Jaramillo-Botero, [iD] [a] Xue-hai Ju [iD] [b] and
William A. Goddard III [iD] *[a]

We developed a new coarse-grained (CG) molecular dynamics force field for polyacrylamide (PAM) polymer based on fitting to the quantum mechanics (QM) equation of state (EOS). In this method, all nonbond interactions between representative beads are parameterized using a series of QM-EOS, which significantly improves the accuracy in comparison to common CG methods derived from atomistic molecular dynamics. This CG force-field has both higher accuracy and improved computational efficiency with respect to the OPLS atomistic force field. The nonbond components of the EOS were obtained from cold-compression curves on PAM crystals with rigid chains, while the covalent terms that contribute to the EOS were obtained using relaxed chains. For describing PAM gels we developed water–PAM interaction parameters using the same method. We demonstrate that the new CG-PAM force field reproduces the EOS of PAM crystals, isolated PAM chains, and water–PAM systems, while successfully predicting such experimental quantities as density, specific heat capacity, thermal conductivity and melting point.

Introduction

Polyacrylamide (PAM) is a water-soluble polymer synthesized from acrylamide sub-units. Due to its significant thickening and flocculating effects in water, PAM is widely used in enhanced oil recovery,[1–3] water treatment,[4–6] soil conditioning[7–9] and biology laboratories.[10–13] The PAM chain structure contains a hydrophobic polypropylene backbone plus a crowded hydrophilic pendant amide group for each monomer on the chain. The strong backbone keeps the PAM chains stable from hydrolysis, while the polar amide groups provide strong interactions with water molecules. As a result, PAM can significantly improve the rheology of water while stabilizing aqueous gels at very low concentrations. This capability is leading to novel experimental and computational efforts to extend its applications.

To understand and modify the properties of macromolecular materials, experimental and computational investigations are both important. Compared to experiments, computational

[a] Materials and Process Simulation Center, California Institute of Technology, Pasadena, California 91125, USA. E-mail: wagoddard3@gmail.com

[b] Key Laboratory of Soft Chemistry and Functional Materials of MOE, School of Chemical Engineering, Nanjing University of Science and Technology, Nanjing 210094, P. R. China

† Electronic supplementary information (ESI) available. See DOI: 10.1039/d0cp05767c

simulations provide new atomistic insights and theoretical understanding connecting the dynamics of structure evolution and atomistic level interactions to provide critical cues to steer property-design and modifications. However, such computations face a dilemma: either use high accuracy methods for restricted length and time scales or use simplified less accurate methods for large-scale systems that provide compromised atomistic information. This is particularly relevant in polymer modelling, because their properties depend on micro-scale configurations that are beyond practical atomistic simulations. For example, Khabaz and co-workers found that the intrinsic viscosity of dilute polymer depends on the shape and size of the chains: linear- and comb-shaped chains (with branch frequencies of 10–100 nm) exhibit 50% higher viscosity than H- and star-shaped chains.[14] Their branching frequencies are 10–100 nm^{-1} in order to obtain the topologies of the chains.

In general, characteristic time scales (τ) for atomistic bonds and angles are on the order of ~ 0.1 picosecond (ps) while torsional time scales in $\tau \sim 10$ ps. Therefore, polymers with degrees of polymerization higher than their entanglement lengths require very long relaxation times, typically many orders of magnitude beyond the scale of atomistic simulations. This problem becomes worse at lower temperatures, near the polymer glass transition temperature.

In order to alleviate this problem, molecular dynamics simulations use coarse grain (CG) models that filter the high-frequency

This journal is © the Owner Societies 2021

Phys. Chem. Chem. Phys., 2021, **23**, 10909–10918 | 10909

vibrational modes to enable longer integration timesteps, larger-scale models, and a smoother potential energy surface.[15–18] CG models merge groups atoms to effectively ignore the high frequency inner-group interactions while tracking longer range interactions. This enables CG models to describe much larger space and time scales, at the expense atomistic accuracy. The development of CG molecular force fields has mostly been based on fits of derived properties to experiment or to atomistic molecular dynamics (MD) distributions. These MD atomistic models are in turn approximations to the true quantum mechanical potential energy surfaces of a particular system. For example, Lei and Pallavi developed their CG-PAM models using dissipative particle dynamics (DPD) and iterative Boltzmann inversion (IBI) strategies, respectively.[19,20] The DPD is a highly simplified bead-spring model with the interactions described by empirical equations. The IBI method focuses on reproducing microscopic observables (*e.g.*, bonds and angle distributions) of a system according to atomistic dynamics from simulations using existing atomistic force fields. In general, the accuracies of such CG models are limited by the inherent inaccuracy and limited transferability of the empirical parameters of the atomistic force fields.

Karimi-Varzaneh *et al.* compared various coarse-grained models developed by different techniques and mapping schemes for amorphous polystyrene.[21] They concluded that the use of CG force fields developed from equilibrium atomistic models in nonequilibrium simulations are possible, providing reliable results for both structural and dynamical properties, including shear viscosity. However, the transferability over thermodynamic states different from that used in the reference atomistic simulations for structure-based CG force fields seems to be erratic and difficult to predict, except for the conditional reversible work (CRW) method. Unlike the IBI method,[22] the CRW method averages over all atomistic degrees of freedom of a local sub-system to avoid the distribution bias from a specific thermodynamic state.

Another widely used empirical CG model is MARTINI force field that was developed for biosystems but recently extended to non-biosystems.[23] The key feature of the MARTINI CG model is its systematic parametrization based on thermodynamic data, especially experimental partitioning data. However, such experimental data may not be available to develop CG force field for new systems.

Aside from the empirical approach to force field development, there have been important contributions to the development of molecular force fields from quantum mechanics (QM) calculations. For example, Grimme proposed a black-box type procedure (QMDFF) to generate classical potential energy functions from QM input data.[24] Cacelli *et al.* parametrized intramolecular force fields by using the energy and its first and second geometrical derivatives obtained from Density Functional Theory (DFT) calculations for a number of conformations of a single molecule.[25] Brunken *et al.* recently developed and combined an automatically parametrizable quantum chemically derived molecular mechanics model with machine-learned corrections under autonomous uncertainty quantification and refinement.[26] These methods show that QM calculations provide a robust source for developing molecular force field (FF).

Here, we report a new approach to develop accurate CG-FF, and demonstrate it for PAM, QM-CG-PAM. This approach is based on quantum mechanics equations of state (QM-EOS) for polymer crystals. First, we explain the approach and demonstrate that it provides an improved compromise between accuracy and coarsening level compared to existing state-of-the-art CG approaches. Then we validate the QM-CG-PAM model by showing that it reproduces experimental observables for PAM. Then we show how it can be used to develop CG force fields for other polymer systems. Compared to the IBI, DPD, CRW and QMDFF strategies, our quantum mechanics coarse graining equation of state (QM-CG-EOS) approach is low-cost, easy-to-implement, and flexible.

Computational methods and details

Parameterization of QM-CG-PAM force field

All QM computations for the EOS of PAM crystals were performed using the Vienna ab initio Simulation Package (VASP)[27] using the PBE flavour of the Generalized Gradient Approximation level for DFT and including the Grimme–Becke–Johnson D3 dispersion corrections.[28,29] We showed recently that this PBE-D3 DFT leads to accurate EOS for molecular crystals up to 100 GPa or higher.[30] We generated the QM-EOS as cold-compression/expansion curves and then mapped these onto a CG representation as depicted in Fig. 1. QM-EOS avoids thermodynamic state bias through the cold-compression/expansion because QM-EOS describes the interactions for states ranging from highly compressed bulk to gas.

For PAM, we considered two crystal configurations:

• CRY1 contains hydrophilic–hydrophilic and hydrophobic–hydrophobic interactions between the chains.

• CRY2 contains hydrophilic–hydrophobic interactions between the chains.

EOS were generated for each case.

These EOS considered periodic crystals obtained by compressing and stretching along the lattice directions without changing the intrachain bond distances angles or chain-orientation.

Fig. 2 and Table 1 show the QM-geometry-optimized PAM crystals. Every crystal contains 2 chains with 4 monomers. The mapping scheme and crystal structures chosen comply with the four conditions that must be fulfilled in coarse-graining process, as proposed by Riniker:[31]

(1) Non-essential degrees of freedom and interactions unrelated to the process or property of interest are removed.

(2) The CG must enable simulations on very large systems, so that the computational gain is sufficiently substantial to offset the loss in accuracy.
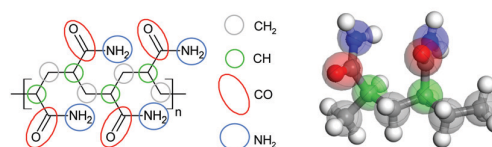

Fig. 1 Coarse-grain mapping scheme for polyacrylamide (left) and atomistic representation (right). Each bead is located at the center of mass of the corresponding atomic group.

10910 | *Phys. Chem. Chem. Phys.*, 2021, **23**, 10909–10918
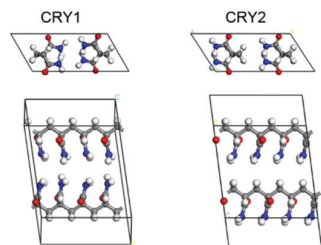
This journal is © the Owner Societies 2021

Fig. 2 Optimized crystal structures of polyacrylamide. CRY1 has hydrophilic–hydrophilic and hydrophobic–hydrophobic interactions. CRY2 has only hydrophilic–hydrophobic interactions. The upper figures show the view perpendicular to the chain axis. The lower figures show the side view. Grey = carbon, red = oxygen, blue = nitrogen, white = hydrogen.

Table 1 Optimized lattice parameters of polyacrylamide crystals. Units are Angstrom and degree

Structure	a	b	c	α	β	γ
CRY1	10.25	13.63	6.15	123.64	94.05	97.26
CRY2	10.24	13.52	6.01	119.74	90.85	97.92

(3) The interactions governing the degrees of freedom to be eliminated should be largely decoupled from the interactions governing the other degrees of freedom of the system that are to be maintained. This means that the frequency components of the motions along the degrees of freedom to be eliminated must be well separated from other frequencies in the system and that the coupling between the two types of motions is weak.

(4) Elimination of the fast motions should allow simple, efficient representations of the interactions governing the other, remaining degrees of freedom.

In our CG-PAM model, the C–H, N–H, C=O bonds and the H–C–X, H–N–X, O=C–X (X represents C, H, O or N atom) angles are eliminated to meet the above conditions. These bonds and angles are not essential for the shape of the polymer chain, nor the entanglement between different chains, so condition (1) is met. The H atoms requires much smaller timestep and more computational resources in simulations, so they are merged into heavy atoms, satisfying condition (2). The CRY1 crystal configurations has the hydrophobic edges of adjacent acrylamide chains in contact, as well as the hydrophilic edges. Thus, we can separately obtain EOS for the hydrophobic–hydrophobic and for hydrophilic–hydrophilic interactions. The CRY2 crystal configurations has the hydrophobic edges of one acrylamide chains in contact the hydrophilic edge of the adjacent chain, which serves to describe the hydrophobic–hydrophilic EOS. These chain–chain interactions eliminate degrees of freedom that are largely decoupled from the others. For example, CH and CC bonds have much larger frequencies than the non-bond interactions, fulfilling conditions (3) and (4).

Hydrogen bonds (HB) are particularly important for the PAM model, because they contribute to the polar interactions found in PAM dynamics. HBs are very orientation-dependent, with Morozov[32] indicating that the HB in the dimer prefers H-bond angle $>150°$. The HBs in our benchmark system are 148°, 169°,

167° and 138° for HBs in CRY1, and 156°, 155°, 155° and 156° for HB in CRY2. Thus, the CRY1 and CRY2 structures properly describe typical PAM interactions.

To fit the QM-EOS of these crystals, we describe the non-bond interactions between the beads using Morse two-body potentials (eqn (1)).

$$E_{vdW} = D_0\{\exp[-2\alpha(r - r_0)] - 2\exp[-\alpha(r - r_0)]\} \qquad (1)$$

Here we consider that our EOSs emphasize properly the different CG interactions.

The CG level calculations were performed using the LAMMPS Molecular Dynamics Simulator.[33] The parameters for the nonbond interactions (referred to here as van der Waals, vdW) were adjusted to fit the five QM EOS. QM energies were obtained for all chains while keeping the chains rigid as the lattice parameters were changed.

To obtain bond and angle interactions between the beads for our CG-PAM model, we constructed a single chain of 10 acrylamide monomers, shown in Fig. S1(a) (ESI†). Then we used QM to independently examine the energies for stretching the bonds and for bending the angles using PBE-D3. There were fitted to obtain Harmonic potentials (eqn (2) and (3)) for the bonds and angles of the CG-PAM. The fit is shown in Fig. S1(b–g) (ESI†).

$$E_{bond} = K_B(r - r_0)^2 \qquad (2)$$

$$E_{angle} = K_A(\theta - \theta_0)^2 \qquad (3)$$

We then derived nonbond vdW interaction parameters between water and PAM based on QM calculations at the DFT-PBE-D3 level. Because the SPC-E water model predicts accurate values for viscosity and heat of evaporation, we selected SPC-E to describe water–water interactions.[34] This water model contains three charge sites but only one van der Waals site (centred at the oxygen atom). Our coarsening of the water–PAM interactions uses the bead located at the oxygen as the vdW site for the water molecule. The PAM–water interaction is also described by eqn (1), where the parameters D_0, α and r_0 were optimized to fit the QM-EOS of the water–PAM adsorption structures. To obtain explicit interaction parameters between the water and PAM beads, we built models of isolated acrylamide monomers with a single water molecule adsorbed at various sites. These sites were chosen to represent the interaction for only one pair of beads, to allow optimization of parameters for one pair at a time. The equilibrium position in each EOS corresponds to a local energy minimum of the optimized structure. Based on these EOS, the nonbond parameters for water–PAM were obtained by considering the correlations of the water bead–PAM bead distances and QM energies.

Validation of optimized CG-PAM force field

Using our CG-PAM model for a system of 20 chains each with 100 PAM monomers, we carried out MD with our optimized QM-CG-PAM force field to predict physical properties that we compared to experimental data and to the OPLS atomistic force field.[35]

To obtain an equilibrated polymer model, we built the initial structure at a low density (0.6 g cm^{-3}) and performed a series of

This journal is © the Owner Societies 2021

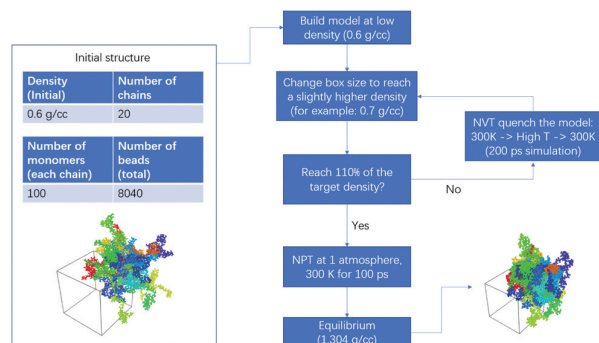Phys. Chem. Chem. Phys., 2021, 23, 10909–10918 | 10911

Fig. 3 The construction and equilibrium procedure of the CG-PAM model.

''compress-quench'' iterations heating the system up to 800 K and back down to 300 K. This led to a converged target density of 1.3 g cm^{-3}, as shown in Fig. 3 and Fig. S3 (ESI†). We kept the melting point near the centre temperature of the quenching cycle to improve equilibration. Our simulations shows that the last 0.1 ns NPT equilibrium is sufficient to converge the density and potential energy (Fig. S4, ESI†). This procedure allows the chains to entangle optimally with each other.

We integrated the isobaric molecular dynamics (NPT) ensemble equations of motion for the CG-PAM model using a 5 fs integration timestep with a Nose–Hoover thermostat (damping time of 500 fs) and a Nose–Hoover barostat (pressure damping time of 5 ps). The NPT simulations were performed for 1 ns at various temperatures in the range of 300–750 K with 1 atmosphere pressure. We then calculated experimental observables such as density, heat capacity, and melting temperature.

We built and simulated an equivalent-sized PAM atomistic model using the OPLS force field for comparison.[35] A timestep of 1 fs, a temperature damping time of 100 fs and a pressure damping time of 1 ps were used for the atomistic simulations, while other settings remained the same as those in the CG model.

Using our optimized the water–PAM interactions, we simulated aqueous gel models consisting of PAM and water with concentrations of 40, 60 and 80% PAM by weight. These were built and relaxed using the same procedure as for pure CG-PAM. The amount of CG-PAM was kept constant at 20 chains each with 100 monomers, while the amount of water molecules was set to 2000, 5300 and 11 900 to reach the PAM weight concentrations of 40, 60 and 80%, respectively. Using our optimized CG-PAM force field and water–PAM interactions, we carried out 1 ns NPT dynamics simulations to calculate such observables as density, specific heat capacity, and thermal conductivity for three concentrations. The same simulations were performed on atomistic models using the OPLS force field for comparison.

All dynamics for PAM aqueous gels were done at 300 K and 1 atmosphere pressure using the NPT ensemble, Nose–Hoover thermostat and barostat with 1 fs timestep, 100 fs temperature damping time and 1 ps pressure damping time.

We then used the CG-PAM force field to predict shear viscosities using a SLLOD deformation scheme under non-equilibrium molecular dynamics (NEMD) simulations.

Results and discussion

Parameterization of van der Waals interactions

To obtain EOS of the PAM crystals, the deformations increased one cell parameter at a time. This helps identify which CG pair is responsible for the change in energy. All pairs of non-bond interactions contribute to each EOS, so that a single set of parameters will not agree exactly with all the QM-EOS. Fig. 4 shows the a, b, c, d and e EOS involve mainly $NH_2 \cdots NH_2$, $CH_2 \cdots CH_2$, $NH_2 \cdots CH_2$, $CO \cdots NH_2$ and $CO \cdots NH_2$ non-bond interactions respectively. The relative energies are referenced to the energies of the crystal expanded by 2 nm in each direction. The minimum points are global energy minimum. The atomistic simulations were carried out with the atoms located at exactly the same positions as the QM models, calculated as single point energies. We obtained the non-bond parameters (Table 2) for the beads as the best fit over all 5 QM-EOS, based on the least squares error against all QM-EOS shown in Fig. 4.

Both our CG force field and the atomistic OPLS force field lead to good minimum-energy lattice parameters, i.e., accurate densities. Nonetheless, the atomistic OPLS force field overestimates the hydrophilic interactions (by 35%) but underestimates the hydrophobic ones (by 39 to 58%), which leads to an incorrect well depth. In contrast, our CG force field agrees well with QM in terms of binding energy (2 to 17% deviation). This implies that the CG force field should be more accurate than OPLS for energy-dependent properties, such as melting point, heat capacity and thermal conductivity.

Due to the important applications of PAM as a water thickener, we calculated three different EOS related to the material's rheological behavior. These EOS were only used for validation, not parameter optimization. In Fig. 5(a and b), the CG and OPLS force field show barriers 20–40% lower than the QM-predicted EOS. In order to avoid bad contacts between the chains, we allowed the cell size of the non-chain-directions to adjust during the translation. The side group is flexible while the backbone is rigid. This represents the chain–chain friction more realistically. The CG and the OPLS force field underestimate the friction between the chains having hydrophilic–hydrophilic contacts and hydrophobic–hydrophobic contacts. For the rotation barrier, the CG force field is in good agreement with the QM friction EOS and slightly better than OPLS (Fig. 5(c)).

The non-bond interactions parameters between water and CG-PAM were developed for aqueous gel simulations using the QM-EOS of the water-monomer adsorption structures as shown in Fig. 6. From coupled cluster calculations using MP2/aug-cc-pVXZ, there is a −6.36 kcal mol^{-1} for $NH_3 \cdots H_2O$ hydrogen-bond-affinity, while our DFT-D3 leads to −6.15 kcal mol^{-1} for $R-NH_2 \cdots H_2O$.[36] On the other hand, the OPLS atomistic force field predicts a difference of about 4 kcal mol^{-1} for the hydrogen bond. Again, the atomistic OPLS force field overestimates the hydrophobic interaction and underestimates the hydrophilic interactions. Sometimes these deviations cancel each other out, but they may still contribute to errors in the calculation of energy-dependent properties. By fitting to the QM-predicted EOS, the optimized CG force field (parameters in Table 3) is more accurate than OPLS in reproducing the potential energy curve, representing an improvement for aqueous PAM gel models and simulations.
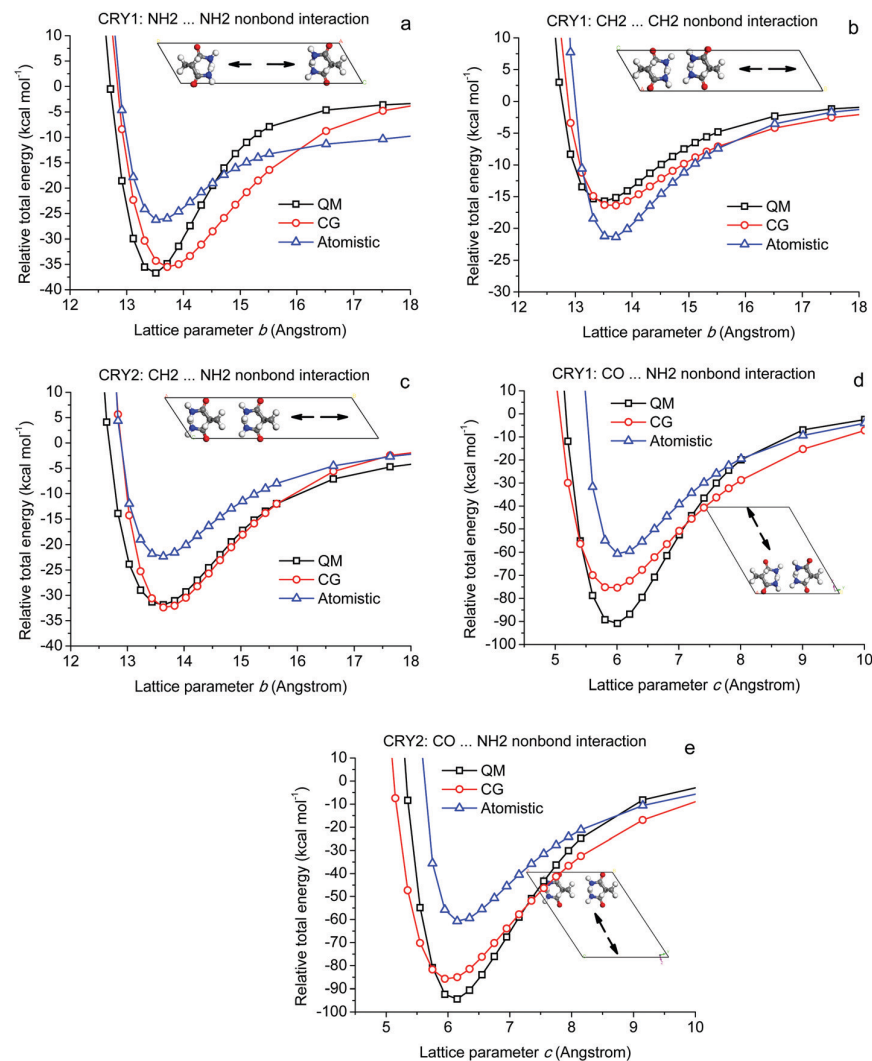
10912 | *Phys. Chem. Chem. Phys.*, 2021, **23**, 10909–10918

This journal is © the Owner Societies 2021

Fig. 4 Five EOS based on changing various cell parameters for PAM crystals while keeping the chains rigid. The arrows represent the stretching directions of the crystals. Here atomistic is OPLS.

Table 2 Optimized Morse parameters for the CG-PAM non-bond interactions

Non-bond interaction	D_0 (kcal mol^{-1})	α	r_0 (Å)
CH$_2$–CH$_2$	0.1141	1.4170	4.2771
CH$_2$–CH	0.1141	1.4170	4.2771
CH$_2$–CO	0.3258	1.3083	4.0052
CH$_2$–NH$_2$	0.3327	1.2306	4.4548
CH–CH	0.1141	1.4170	4.2771
CH–CO	0.3258	1.3083	4.0052
CH–NH$_2$	0.3327	1.2306	4.4548
CO–CO	0.9307	1.1995	4.4345
CO–NH$_2$	0.9503	1.1218	3.8019
NH$_2$–NH$_2$	0.9702	1.0441	3.9663

Parameterization of valence interactions

The valence parameters (Table 4) in CG-PAM were optimized using QM-predicted energy curves following the same strategy as for the non-bond parameters. The comparison between QM,

CG and atomistic OPLS force field are shown in Fig. 7. Again, our CG force field is more accurate than the OPLS force field, especially for the NH$_2$–CO bond, NH$_2$–CO–CH angle, and CO–CH–CH$_2$ angle. These weaker bonds and angles are all located at the hydrophilic pendant amide groups, while the hydrophobic backbone interactions are fine. This probably affects the properties of OPLS models for PAM aqueous gel.

It's very important to capture the correct polar interactions in PAM and aqueous PAM gel models, because the polar interactions play an important role in thickening and flocculating effects. The interaction between the hydrophilic pendant amide groups determines the cross-linking dynamics of the chains. The water–PAM interactions, especially the water–carbonyl and water–amino interactions, are the main contributors to the solubility and rheology of PAM in water. Therefore, accurate polar interactions enable an improved understanding of aqueous PAM gels.
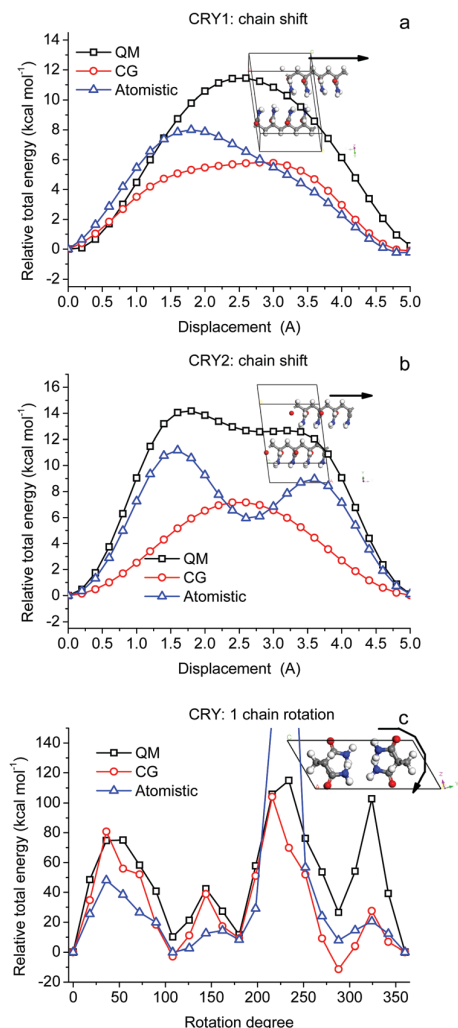
This journal is © the Owner Societies 2021

Phys. Chem. Chem. Phys., 2021, **23**, 10909–10918 | **10913**

Fig. 5 EOS for translation of a single one chain in CRY1 (a) and CRY2 (b) and the EOS of rotation of one chain in CRY1 (c).

Fig. 6 EOS of water–PAM non-bond interactions.

Validation against experimental observables

The best validation of the accuracy of a simulation is to compare against the corresponding experimental observables. First, we focus on the melting point, an important property for polymers. The *NPT* dynamics simulations for CG-PAM and atomistic PAM were performed at various temperatures to obtain the time-averaged density and potential energies, as functions of temperature. Since the temperature dependence of the properties change at the phase transition, we located the melting points at the turning points of these functions. From Fig. 8(a and c), based on potential energies, it is hard to find their inflection points. This is because of the energy fluctuations of the amorphous structures. Notwithstanding, we can locate this transition point by piecewise linear interpolation. Because the experimental melting point is about 520 K, we assigned the points below 520 K as solid and above 520 K as liquid. Then we did a linear fit for the temperature dependence for the 2 sets of points to locate the melting point at the line crossing.
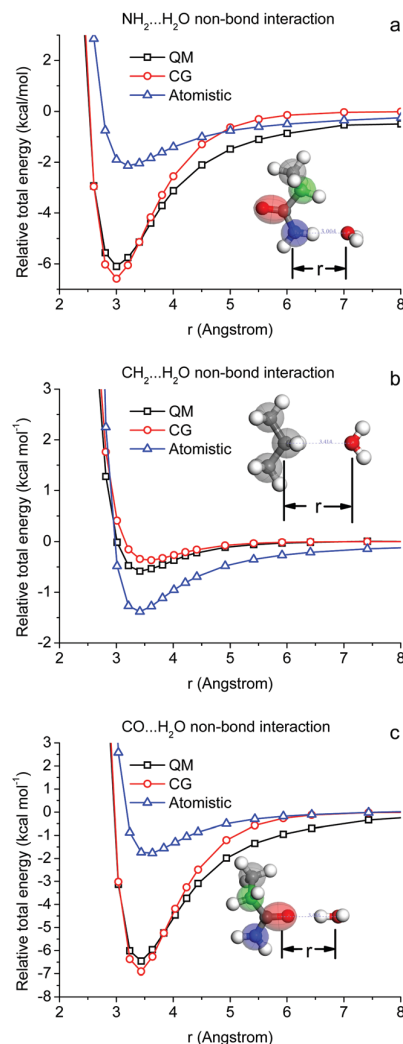
Table 3 Optimized water–PAM non-bond interaction parameters

Pair	D_0 (kcal mol^{-1})	α	r_0 (Å)
NH$_2$–H$_2$O	4.0400	1.5446	3.0743
CH$_2$–H$_2$O	0.3707	1.6415	3.5594
CH–H$_2$O	0.3707	1.6415	3.5594
CO–H$_2$O	6.5006	1.5277	3.4281

Table 4 Optimized valence parameters for CG-PAM

Bond or angle	K_B or K_A (kcal mol^{-1})	r_0 or θ_0 (Å or degree)
CO–NH$_2$	398.12	1.9515
CH–CO	286.11	2.0788
CH–CH$_2$	295.66	1.6649
CH–CO–NH$_2$	499.08	82.72
CH$_2$–CH–CO	122.39	99.34
CH$_2$–CH–CH$_2$	111.35	108.19
CH–CH$_2$–CH	111.51	107.69

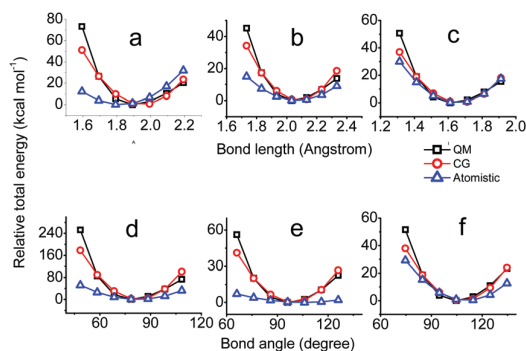The estimated melting points by CG-PAM (517–530 K) and atomistic PAM (553 K). Comparing with the experimental melting

10914 | *Phys. Chem. Chem. Phys.*, 2021, **23**, 10909–10918

This journal is © the Owner Societies 2021

Fig. 7 EOS of valence interactions, where (a, b and c) are NH$_2$−CO, CO− CH and CH−CH$_2$ bonds, respectively. Lower figures (d, e and f) are NH$_2$− CO−CH, CO−CH−CH$_2$ and CH−CH$_2$−CH angles, respectively. Generally, the CG is much closer to QM than OPLS.

point 519–523 K, our CG-PAM model is more accurate.[37] The densities of both CG-PAM (1.304 g cm^{-3}) and OPLS PAM (1.307 g cm^{-3}) are in good agreement with experiment (1.30 g cm^{-3}), but their thermal expansion behaviours are slightly different. The OPLS model for PAM has a lower density at high temperatures, probably because it underestimates vdW well depths for hydrophilic groups as discussed in Section 3.1. In addition, we calculated the densities and melting points for CG-PAM melt models with chain lengths of 2, 4, 8, 16, 32, 64, 128 monomers, as shown in Fig. S6 (ESI†). The densities and melting points are in the range of 1.01–1.29 g cm^{-3} and 472–530 K, respectively.

Our second validation is for heat capacity. The time-averaged enthalpies at different temperatures were calculated, leading to the specific heat capacities (C_p) shown in Fig. 9. The OPLS PAM model shows 1.5 times larger C_p than experiment. This may arise from the too-weak hydrophilic interactions. In contrast, the C_p of CG-PAM model (1.45 kJ kg^{-1} K^{-1}) is ∼15% smaller than experiment (1.75 kJ kg^{-1} K^{-1}).[38] We find similar behaviours for the aqueous PAM gel at 300 K as shown in Fig. 9(b).

The remaining validations focus on the concentration dependence of density and thermal conductivity. Fig. 10(a) shows that the density of CG-PAM aqueous gel (1.123 g cm^{-3}) agrees with experiment (1.138 g cm^{-3}) at a concentration = 0.4. In contrast, the OPLS model leads to 10% larger density at the same concentration, probably due to the inaccurate water–PAM non-bond interactions shown in Fig. 6.

The thermal conductivities were calculated using the Green–Kubo (GK) formulation that averages the auto-correlation of the heat flux. Both the CG and OPLS models produce thermal conductivities higher than experiment,[38] but the CG model shows better accuracy than the OPLS model.

From the above validations, this QM based CG-PAM force field provides good accuracy for large scale length-time simulations. The accuracy improvement arises from parameterizing directly to QM, while the improved length-scale capability is due to the level of coarsening. For the same size of polymer models, the CG model has a larger mass with reduced interaction terms than the atomistic model. This CG model allows us to use longer timesteps to simulate
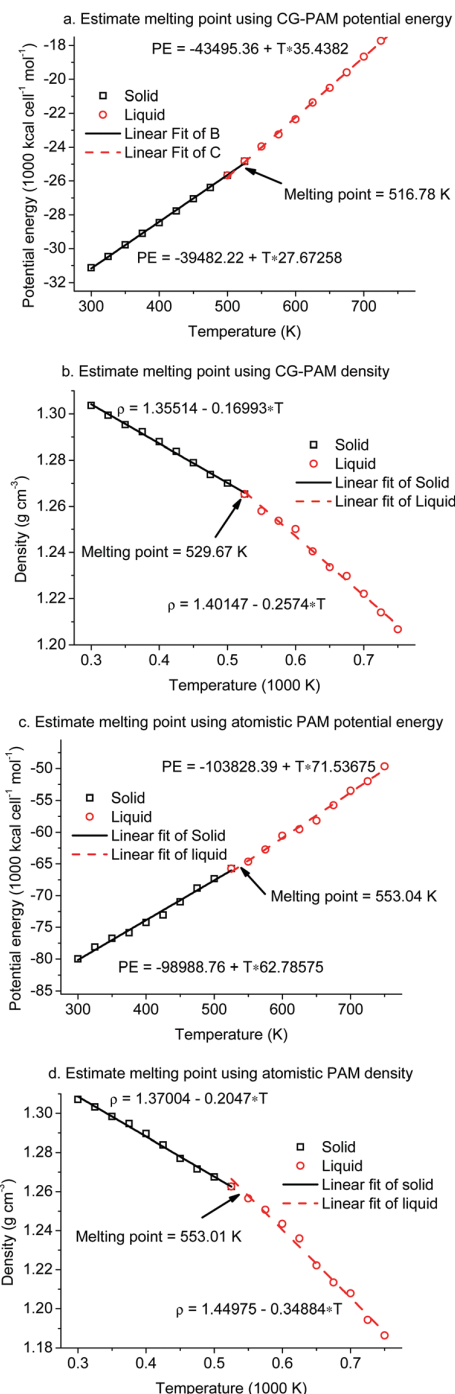

Fig. 8 Estimated melting point using the turning points in the temperature dependence functions of potential energy and density. The experimental melting point of PAM is 519−523 K.[37]

larger models. Comparing with the OPLS atomistic forcefield, our CG-PAM force field uses 2/5 the number of interacting units to represent the atomistic model. We have tested that the simulations are stable at 0–1500 K for timesteps of 5 to 10 fs, which is 5 times longer than the OPLS (usually 1–2 fs). On the whole,
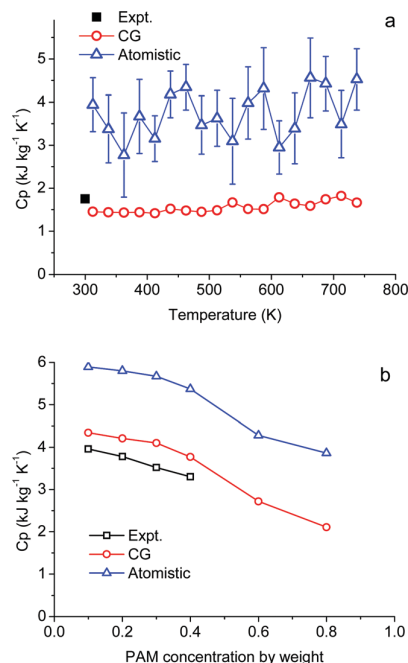
Fig. 9 Temperature dependence of specific heat capacities for pure PAM (a) and concentration dependence of specific heat capacities under 300 K for aqueous PAM gel (b). The error bar in (a) is based on the C_p averaged by 1 ps time interval.
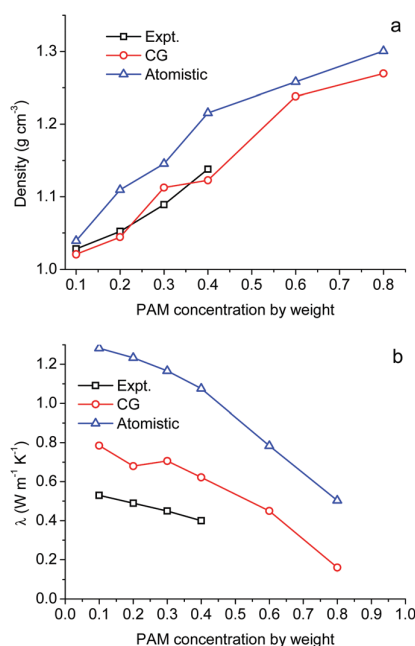

Fig. 10 Concentration dependence on density and thermal conductivity for aqueous PAM gel under 300 K.

the computational efficiency of CG-PAM model is 12.5 times that of atomistic model.

An earlier study shows that hydration free energies of side polar groups depend strongly on the backbone conformation.[39]
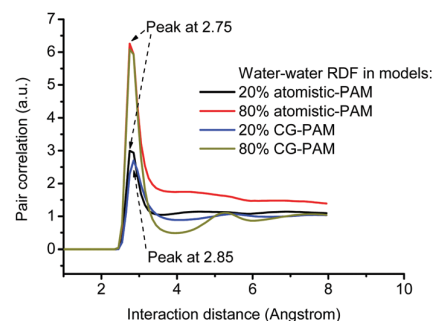

Fig. 11 Water–water radial distribution functions for atomistic and CG-PAM gels with 20% and 80% weight concentrations of PAM. The simulations were performed at 300 K and 1 atmosphere using *NPT* ensemble for 1 ns.

The backbone can strongly affect the affinity for the surrounding solvent. Considering the significance of solvent effects on a PAM gel, we did *NPT* simulations at 300 K and 1 atmosphere on atomistic and CG-PAM gels with 20% and 80% weight concentrations of PAM. The water–water radial distribution functions (RDF) (Fig. 11) show that the CG-PAM enhances the affinity by reducing the water–water distance by 0.1 (from 2.85 to 2.75 Å) Angstrom. The water–water RDF of 80% CG-PAM gel shows a significant valley in range of $r = 3$–5 Å and a peak at $r = 5$–5.5 Å, while that of atomistic-PAM gel does not show these features. This is because of the different level of scattering of the water. From Fig. S5(a) (ESI†), the CG-PAM chains are separated by water.
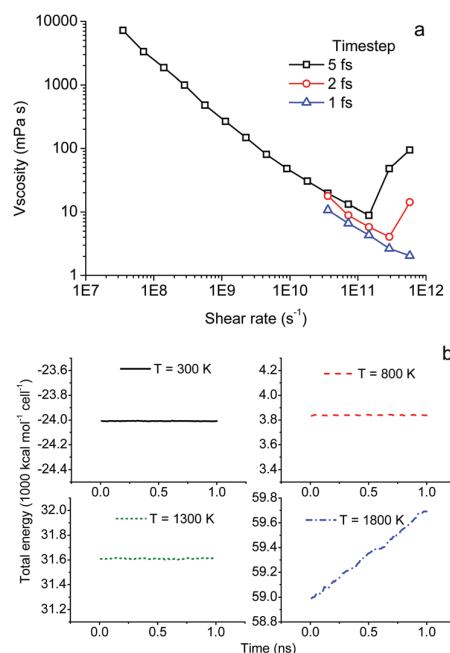

Fig. 12 (a) Shear viscosities as functions of shear rate calculated by different timesteps. The SLLOD-NEMD simulations are performed on 20 chains × 100 monomers CG-PAM models sheared at 300 K. (b) Total energy evolution during *NVE* simulations performed on the CG-PAM melt model with 5 fs timestep and 300–1800 K temperatures.

10916 | *Phys. Chem. Chem. Phys.*, 2021, **23**, 10909–10918

This journal is © the Owner Societies 2021

Since the thickness of the PAM chain is about 5 Å, the locations of the valley and peak are reasonable. However, from Fig. S5(b) (ESI†), the atomistic-PAM chains contact each other leaving cavities for water. So, the RDF of 80% atomistic-PAM shows inverse micelles character, as found in wet octanol or butanol.[40,41] Overall, the different solvent behaviours between CG and atomistic PAM gels results from the weak water–PAM affinity, as found in the atomistic model.

Our CG-PAM model has some limitations. Fig. 12(a) shows the pseudo shear thickening of pure PAM induced by longer timesteps at high shear rates. In the most interesting range of shear rates for polymer simulations, 10^7–10^{11} s^{-1}, the 5 fs timestep is safe. Nevertheless, Fig. 12(b) shows an energy drift at 1800 K, while integration at 5 fs timestep is stable for temperatures lower than 1300 K. In order to retain maximum accuracy, we mapped the CG to a united-atom-like model to limit the simulation scale. We believe this is a good start of the QM-EOS based coarsening methodology that can extend to larger mapping schemes in the future.

Conclusions

Using a QM-derived EOS, we developed a new CG force field for PAM and aqueous PAM gels. This CG force field shows improved accuracy than the well-known OPLS atomistic force field, when compared to both QM-EOS and experimental observables. The CG FF successfully reproduces the EOS of PAM crystals, isolated chains, and water-absorption systems. Compared with the OPLS atomistic force field, our CG FF is more accurate for all validations, including density, heat capacity and thermal conductivity. The melting point is estimated with an error less than 2%. This is unusual for force fields especially CG polymer force fields, because the melting point is sensitive to many structural conditions. Our method starts from the QM EOS, and is parameterized directly from cold compression/expansion EOS on simple idealized crystal models using non-bonded and bonded interactions. We have validated our method on a polymer system that is complicated by the existence of polar interactions, which are not conventionally captured by the standard CG approaches.

Conflicts of interest

There are no conflicts to declare.

Acknowledgements

References

1 P.-S. Kang, J.-S. Lim and C. Huh, *J. Energy Resour. Technol.*, 2020, **143**, 63002–63010.

2 A. Agi, R. Junin, M. Z. Jaafar, R. Mohsin, A. Arsad, A. Gbadamosi, C. K. Fung and J. Gbonhinbor, *J. Mater. Res. Technol.*, 2020, **9**, 13054–13066.

3 Q. Chen, Z. Ye, L. Tang, T. Wu, Q. Jiang and N. Lai, *Polymers*, 2020, **12**, 2130–2136.

4 M. M. Abou-Mesalam, M. R. Abass, A. B. Ibrahim and E. S. Zakaria, *Desalin. Water Treat.*, 2020, **193**, 402–413.

5 Y. Long, X. You, Y. Chen, H. Hong, B.-Q. Liao and H. Lin, *Sci. Total Environ.*, 2020, **703**, 135540–135548.

6 B. Xiong, S. Roman-White, B. Piechowicz, Z. Miller, B. Farina, T. Tasker, W. Burgos, A. L. Zydney and M. Kumar, *J Membr. Sci.*, 2018, **560**, 125–131.

7 Q. Wen, Z. Chen, Y. Zhao, H. Zhang and Y. Feng, *J. Hazard. Mater.*, 2010, **175**, 955–959.

8 J. Lu and L. Wu, *J. Soil Water Conserv.*, 2003, **58**, 270–275.

9 R. E. Sojka, D. L. Bjorneberg, J. A. Entry, R. D. Lentz and W. J. Orts, *Adv. Agron.*, 2007, **92**, 75–162.

10 D. Ochs, *Anal. Biochem.*, 1983, **135**, 470–474.

11 E. E. Charrier, K. Pogoda, R. Li, C. Y. Park, J. J. Fredberg and P. A. Janmey, *APL Bioeng.*, 2020, **4**, 36104–36112.

12 K. E. Maryan, H. S. Lahiji, N. Farrokhi, P. A. Haynes, S. Hamzelou and H. H. Komeleh, *Plant Mol. Biol. Rep.*, 2020, **13**, 1–18.

13 A. Jaramillo-Botero, M. Blanco, Y. Li, G. McGuinness and W. A. Goddard, *J Comput. Theor. Nanos.*, 2010, **7**, 1238–1256.

14 F. Khabaz and R. Khare, *J. Chem. Phys.*, 2014, **141**, 214904–214912.

15 M. Chakraborty, J. Y. Xu and A. D. White, *Phys. Chem. Chem. Phys.*, 2020, **22**, 14998–15005.

16 S. M. Ma, L. Zhao, Y. L. Wang, Y. L. Zhu and Z. Y. Lu, *Phys. Chem. Chem. Phys.*, 2020, **22**, 15976–15985.

17 H. A. Perez-Ramirez and G. Odriozola, *Phys. Chem. Chem. Phys.*, 2020, **22**, 17913–17921.

18 R. Zhou and Y. Q. Gao, *Phys. Chem. Chem. Phys.*, 2020, **22**, 20189–20201.

19 J. C. Lei, S. Xu, Z. Q. Li and Z. S. Liu, *Front. Chem.*, 2020, **8**, 115–127.

20 P. Banerjee, S. Roy and N. Nair, *J. Phys. Chem. B*, 2018, **122**, 1516–1524.

21 H. A. Karimi-Varzaneh, N. F. van der Vegt, F. Müller-Plathe and P. Carbone, *ChemPhysChem*, 2012, **13**, 3428–3439.

22 P. Carbone, H. A. K. Varzaneh, X. Chen and F. Müller-Plathe, *J. Chem. Phys.*, 2008, **128**, 064904.

23 S. J. Marrink, H. J. Risselada, S. Yefimov, D. P. Tieleman and A. H. De Vries, *J Phys. Chem. B*, 2007, **111**, 7812–7824.

24 S. Grimme, *J. Chem. Theory Comput.*, 2014, **10**, 4497–4514.

25 I. Cacelli and G. Prampolini, *J. Chem. Theory Comput.*, 2007, **3**, 1803–1817.

26 C. Brunken and M. Reiher, *J. Chem. Theory Comput.*, 2020, **16**, 1646–1665.

27 J. Hafner, *J. Comput. Chem.*, 2008, **29**, 2044–2078.

28 S. Grimme, J. Antony, S. Ehrlich and H. Krieg, *J. Chem. Phys.*, 2010, **132**, 154104–154110.

29 J. P. Perdew, K. Burke and M. Ernzerhof, *Phys. Rev. Lett.*, 1996, **77**, 3865–3871.

30 S. Naserifar, J. J. Oppenheim, H. Yang, T. Zhou, S. Zybin, M. Rizk and W. A. Goddard III, *J. Chem. Phys.*, 2019, **151**, 154111–154119.

This journal is © the Owner Societies 2021

Phys. Chem. Chem. Phys., 2021, **23**, 10909–10918 | **10917**

31 S. Riniker, J. R. Allison and W. F. van Gunsteren, *Phys. Chem. Chem. Phys.*, 2012, **14**, 12423–12430.

32 A. V. Morozov, T. Kortemme, K. Tsemekhman and D. Baker, *Proc. Natl. Acad. Sci. U. S. A.*, 2004, **101**, 6946–6951.

33 S. Plimpton, *J. Comput. Phys.*, 1995, **117**, 1–19.

34 H. Berendsen, J. Grigera and T. Straatsma, *J. Phys. Chem.*, 1987, **91**, 6269–6271.

35 J. L. Banks, H. S. Beard, Y. Cao, A. E. Cho, W. Damm, R. Farid, A. K. Felts, T. A. Halgren, D. T. Mainz and J. R. Maple, *J. Comput. Chem.*, 2005, **26**, 1752–1780.

36 J. Ireta, J. Neugebauer and M. Scheffler, *J. Phys. Chem. A*, 2004, **108**, 5692–5698.

37 M. Sowwan, S. Makharza, W. Sultan, M. A. Teir and H. Dweik, *Int. J. Phys. Sci.*, 2011, **6**, 6280–6285.

38 Y. Hirata, Y. Kato, N. Andoh, N. Fujiwara and R. Ito, *J. Chem. Eng. Jpn.*, 1993, **26**, 143–147.

39 G. König and S. Boresch, *J. Phys. Chem. B*, 2009, **113**, 8967–8974.

40 B. Chen and J. I. Siepmann, *J. Phys. Chem. B*, 2006, **110**, 3555–3563.

41 G. König, M. T. Reetz and W. Thiel, *J. Phys. Chem. B*, 2018, **122**, 6975–6988.